Supporting Materials for

Surfactant Promoted Solid Amine Sorbents for CO_2 capture

Jitong Wang, Donghui Long*, Huanhuan Zhou, Qingjun Chen, Xiaojun Liu, Licheng Ling*

State Key Laboratory of Chemical Engineering, East China University of Science and Technology, Shanghai 200237

*To whom correspondence should be addressed. E-mail: longdh@mail.ecust.edu.cn; lchling@ecust.edu.cn

This PDF file includes:

1. Characterization of the Sorbents

Nitrogen adsorption/desorption isotherms were measured at 77 K with a Quadrasorb SI analyser. Before the measurements, the samples were degassed in vacuum at 373 K for 12 h. The Brunauer-Emmett-Teller (BET) method was utilized to calculate the specific surface area. The pore size distributions were derived from desorption branch by using the Barrett-Joyner-Halenda (BJH) model. Low-pressure mercury porosimetry was carried out with an AutoPore IV 9500 V1.03 apparatus. The morphology of the samples was observed under scanning electron microscopy (SEM, FEI Q-300) and transmission electron microscopy (TEM, JEOL 2100F).

1.1 TEM images of the HPS support

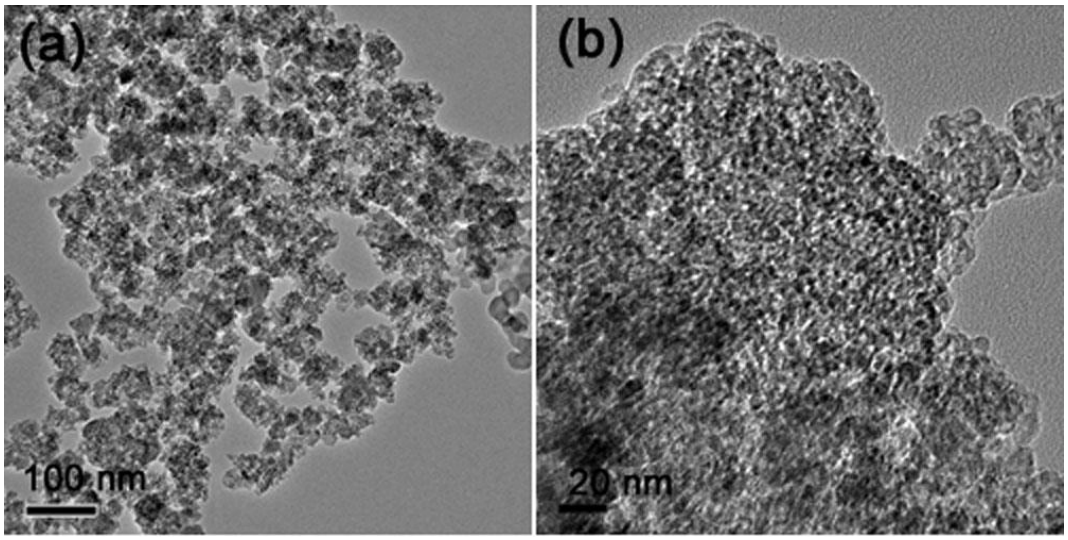

Fig. S1 TEM images of as-prepared hierarchical porous silica (HPS).

TEM images show that the HPS exhibits hierarchically porous structure consisting of the inter-particle large mesopores or macropores and intra-particle wormlike mesopores. The former large pores should be original from the spinodal decomposition during sol-gel process while the latter wormlike mesopores are formed due to the CTAB emulsion templating.

1.2 N_2 adsorption-desorption isotherm and BJH pore size distribution of the support

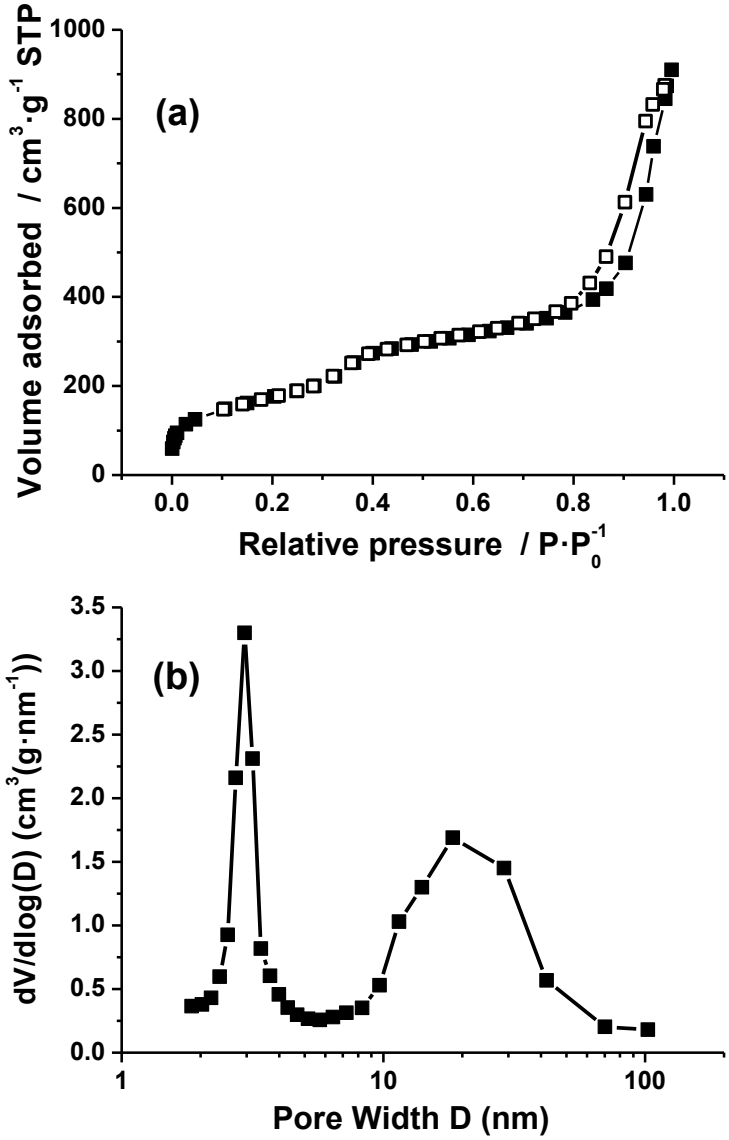

Fig. S2 N_2 adsorption-desorption isotherms (a) and pore size distributions (b) of the hierarchical porous silica support.

The HPS exhibits a type IV adsorption-desorption isotherm according to the classification of IUPAC, indicating the mesoporous structure of the materials. The mesopores are mainly centered at 3 and 15 nm as shown in the pore size distribution curves. The small and large mesopores should correspond to the wormlike mesopores and the inter-particle pore, according to the TEM observation. The HPS has a large BET surface area of 699 m^2/g and a total pore volume of 1.41 cm^3/g.

1.3 Hg porosimetry of the support

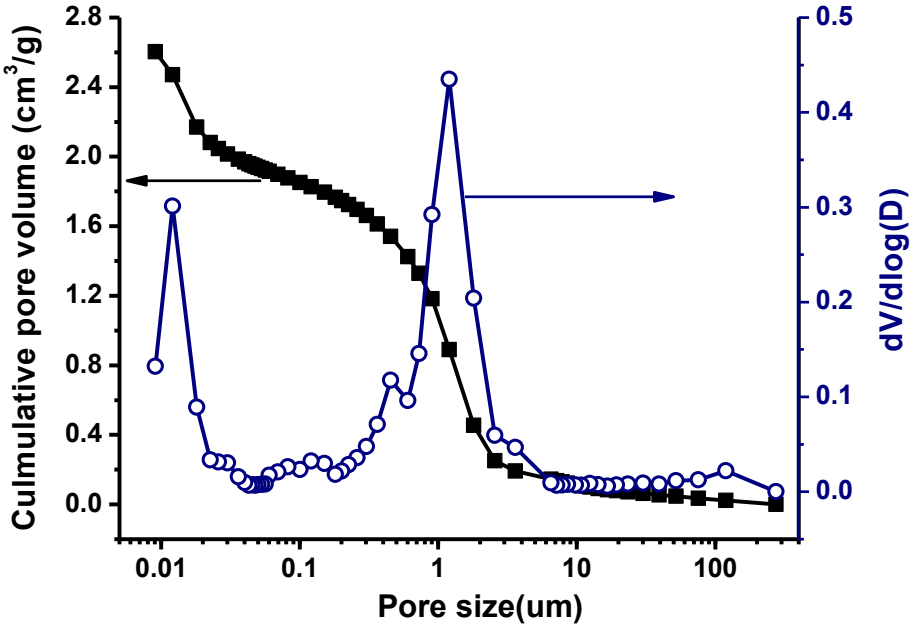

Fig. S3 Cumulative pore volume (a) and pore size distribution (b) of the hierarchical porous silica determined by Hg porosimetry.

The cumulative pore volume curve shows that the total pore volume is about 2.6 cm^3/g. The pore size distribution shows two peaks centered at 15 nm and 1.5 μ m corresponding to the intraparticle mesopores and interparticle macropores, respectively.

1.4 N_2 adsorption-desorption isotherms and BJH pore size distributions of the sorbents

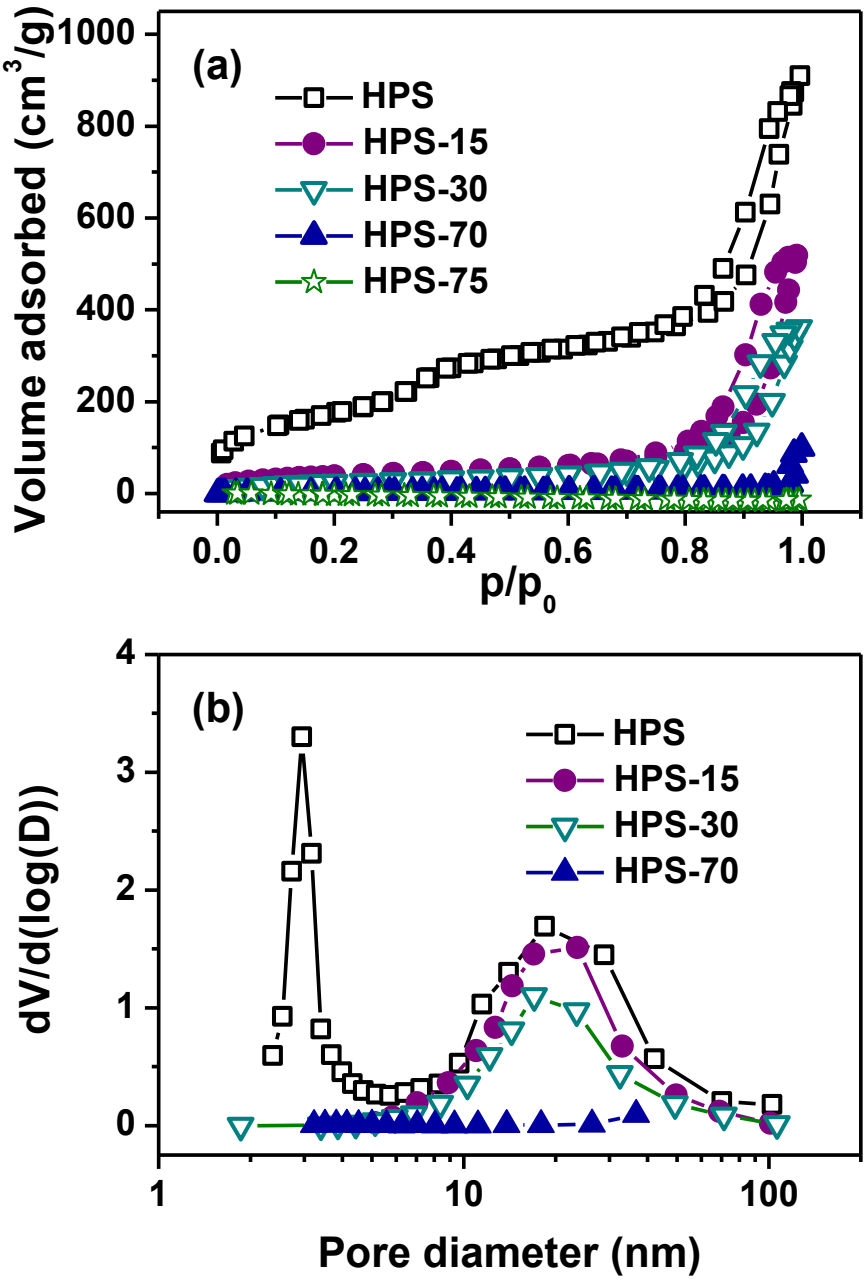

Fig. S4 N_2 adsorption-desorption isotherms (a) and pore size distributions (b) of the hierarchical porous silica sorbents with different PEI loadings.

After PEI loading, the N_2 adsorption capacity decreases greatly with the increase of PEI loading amount, indicating the BET surface area and pore volume decrease. It is noted that the sorbent with 70 % PEI loading has only BET surface area of 10 m^2/g, and even no value is detected for the sample with 75 % PEI loading, suggesting the maximum loading amount is achieved at this level.

Table S1 Porous properties of the hierarchical porous silica sorbents from N_2 adsorption

Samples	S_{BET}[a] (m^2/g)	V_{mic}[b] (cm^3/g)	V_t[c] (cm^3/g)	D_p[d] (nm)
HPS	699	0.08	1.41	17.4
HPS-15	137	0	0.82	17.1
HPS-30	90	0	0.55	16.7
HPS-70	10	0	0.01	16.0
HPS-75	0	-	-	-

[a] BET surface area; [b] micropore volume calculated by t-Plot method; [c] total pore volume; [d] BJH desorption average pore diameter.

1.5 FTIR spectra of the support and the PEI-loaded sorbents

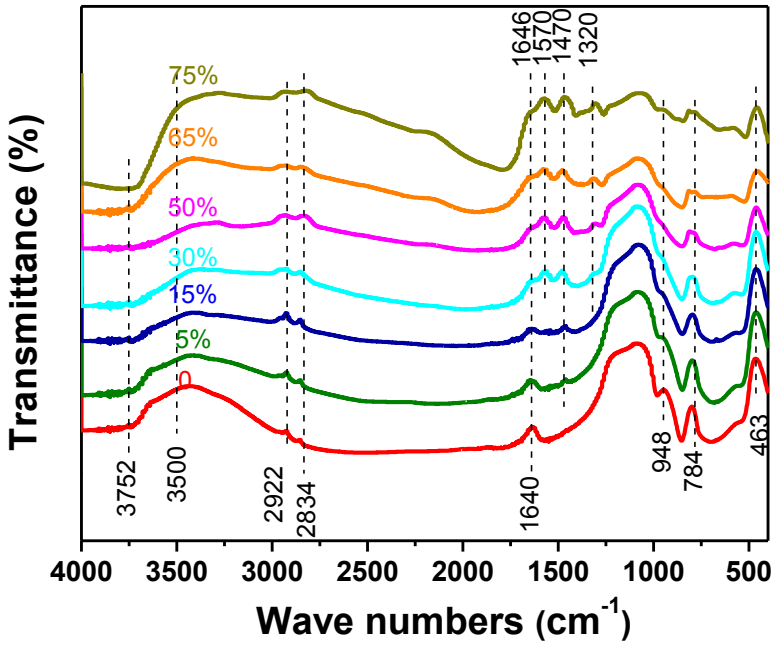

Fig. S5 FTIR spectra of the hierarchical porous silica sorbents with different PEI loadings.

The absorption bands at 1640 cm^{-1} and the broad band at around 3500 cm^{-1} presenting in the IR spectra of HPS are assigned to the stretching vibrations of single Si–OH and hydrogen-bonded Si–OH groups, respectively.[1, 2] With the increase of the PEI loading, the intensity of single Si–OH bond decreases gradually and almost disappears at the PEI loading of 30 wt. %. This result indicates that loaded PEI could shield the stretching vibration of the Si–OH groups due to the possible chemical interaction between them. The bands at 2922 and 2834 cm^{-1} are assigned to the CH_2 stretching modes of the PEI chain.[3] As expected, the intensity of these peaks increases with increasing the PEI loading. In the spectrum of the sorbent, the bands at 1570 and 1470 cm^{-1} are attributed to asymmetric and symmetric bending of the primary amines ($–NH_2$), respectively, while that emerging at 1646 cm^{-1} is assigned to the bending of secondary amines [–N(R)H] in PEI.[4]

However, the values of these peaks reflect a little shift from the normal positions, indicating that there was an interaction between PEI and the internal surface of the porous silica. [5]

2. Dynamic sorption performance of the Sorbents

The dynamic sorption performance of CO_2 on the sorbents was conducted in a fixed-bed flow adsorber operated at 75 ^oC. The fixed bed setup is given in Figure S6. In a typical sorption process, 1 g of the sorbent was packed in the middle of the adsorber supported with quartz wool. The dry or moist CO_2 (99.99 %)/N_2 (99.995 %) gas mixture with a CO_2 mole fraction of 15 % was then introduced through the tube at a flow rate of 50 mL/min. The flow rate of the gas was controlled by electronic flow control instruments. The moisture (80 %RH) was produced by bubbling the gas through water, and the relative humidity was measured by using a hygrometer. The CO_2 concentration in the influent and effluent gas streams was analyzed at regular intervals, using a gas chromatogram (Shimadzu GC-2014) equipped with a thermal conductivity detector (TCD). The sorption capacity of the sorbent was calculated by integration of the area above the breakthrough curve, and from the CO_2 concentration in the inlet gas, flow rate, saturation time, and mass of the adsorbent.

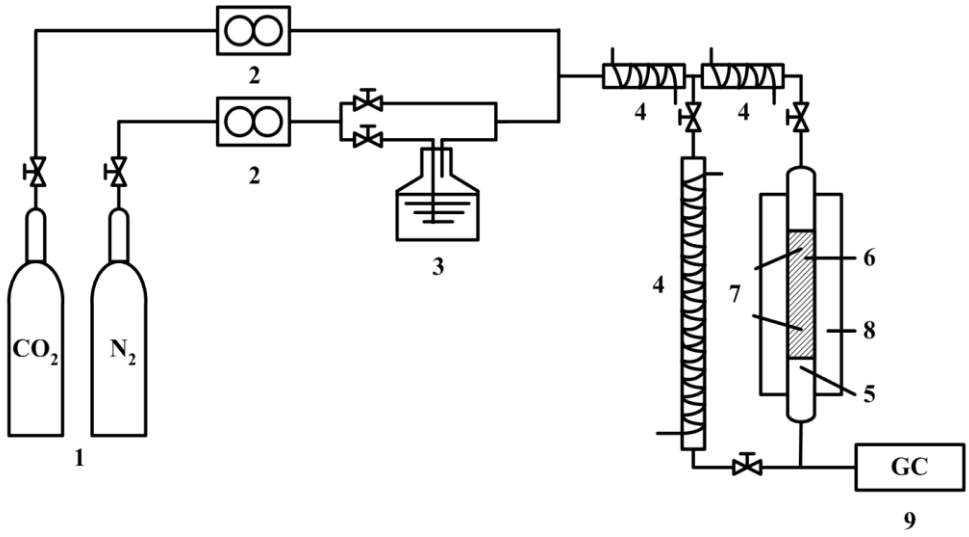

Fig.S6 Schematic diagram of fixed bed setup for CO_2 capture: 1.Gas cylinder, 2. Mass flow controller, 3. Saturator, 4. Heating line, 5. Glass wool, 6. Sample, 7. Temperature probe, 8. Furnace, 9. GC(gas chromatography).

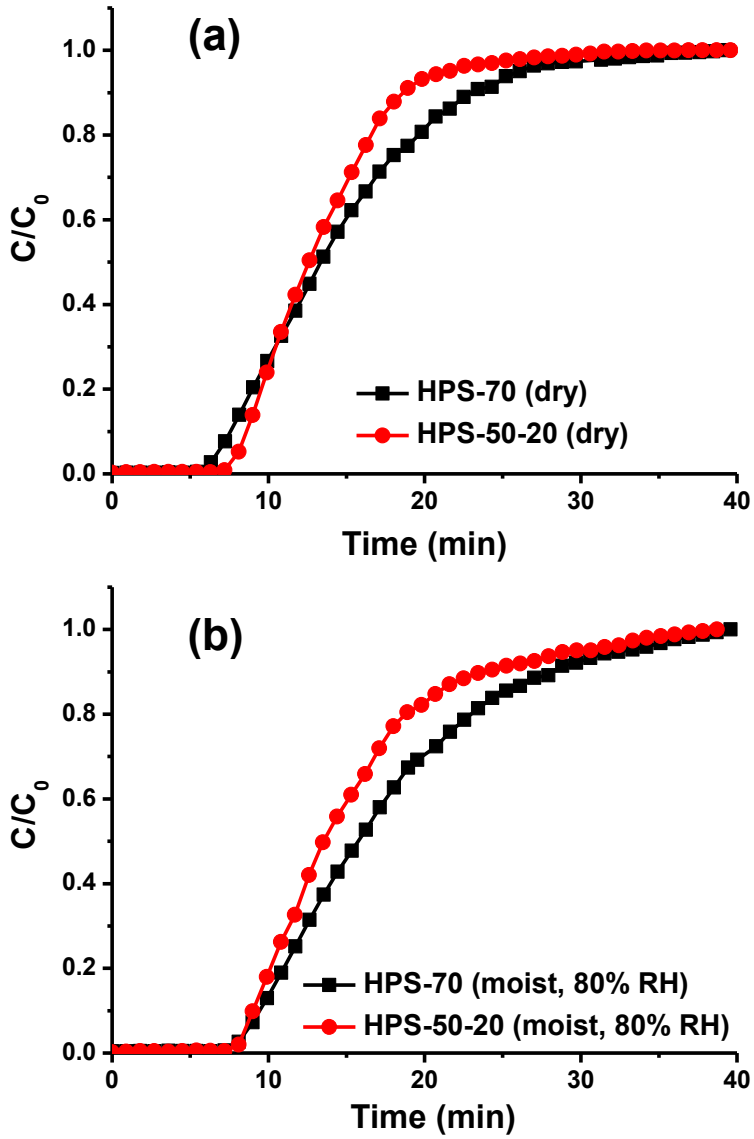

Fig.S7 Breakthrough curves of HPS-70 and HPS-50-20 for dry and moist gas.

Table S2 Dynamic sorption performance of the Sorbents

Samples	Q_B[a] (mg/g)	Q_S[b] (mg/g)	Q_B/Q_S (%)
HPS-70(dry)	112	197	57
HPS-50-20(dry)	143	238	60
HPS-70(moist)[c]	135	181	75
HPS-50-20(moist)[c]	156	212	73

[a] breakthrough CO_2 sorption capacity; [b] saturation CO_2 sorption capacity; [c] CO_2 sorption capacity measured at a relative humidity of 80%.

The dynamic sorption capacity of CO_2 using the fixed-bed adsorption system was measured and shown in Fig. S7. It was found that the surfactant-free sorbent HPS-70 showed a gentle slope, whereas the surfactant-promoted sorbent HPS-50-20 displayed a sharp breakthrough curve. The sorption capacities calculated from breakthrough curves were collected in Table S2.The ratio of breakthrough capacity to total capacity was 57 % for HPS-70 without surfactant, but this value increased to 75 % for HPS-50-20. The result confirmed that the surfactant facilitated the transport of CO_2 leading to fast dynamic CO_2 sorption rate.

When a moist gas mixture was used, the CO_2 breakthrough time increased for both surfactant-free and surfactant-promoted sorbents, confirming that moisture had a promoting effect on the sorption of CO_2. In this work, the improvement of the total capacity in wet condition was found to be around 20 %, independent of the surfactant. The different chemical reactions associated with bicarbonate and carbamate formation are the leading factor for the difference of the CO_2 sorption capacity in dry condition and wet condition.[6, 7]

3. Regeneration performance and thermal stability

3. 1 SEM images of the sorbents before and after CO_2 sorption

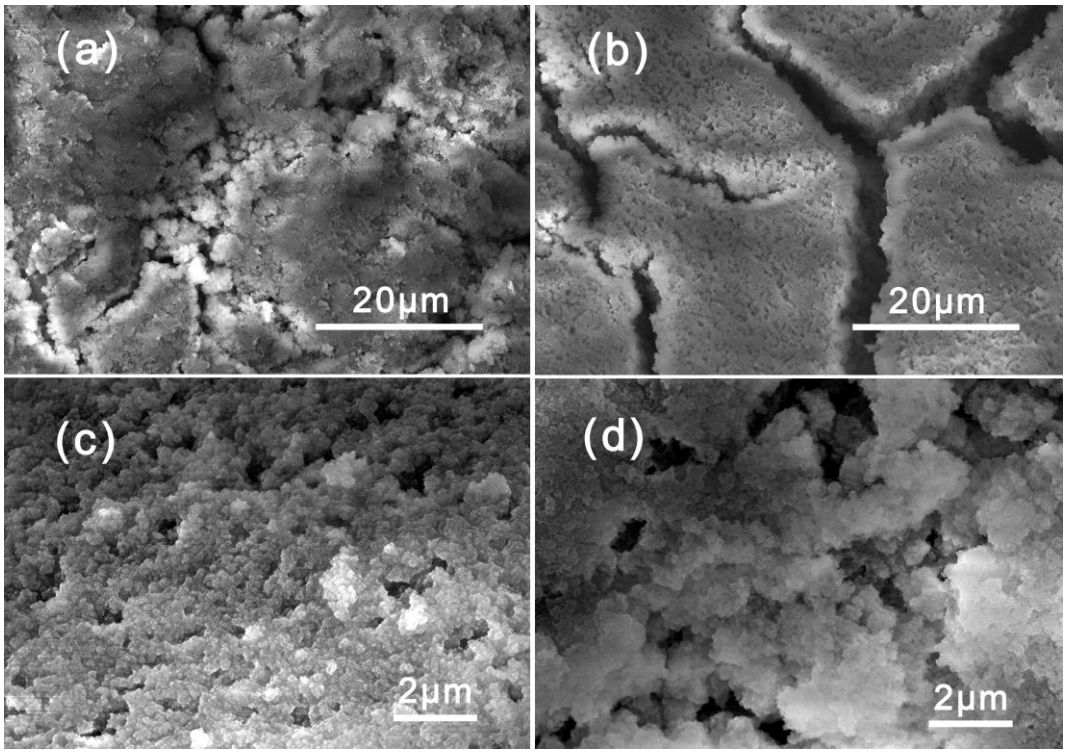

Fig. S8 SEM images of HPS-70 before (a, c) and after (b, d) CO_2 sorption with low and high magnification.

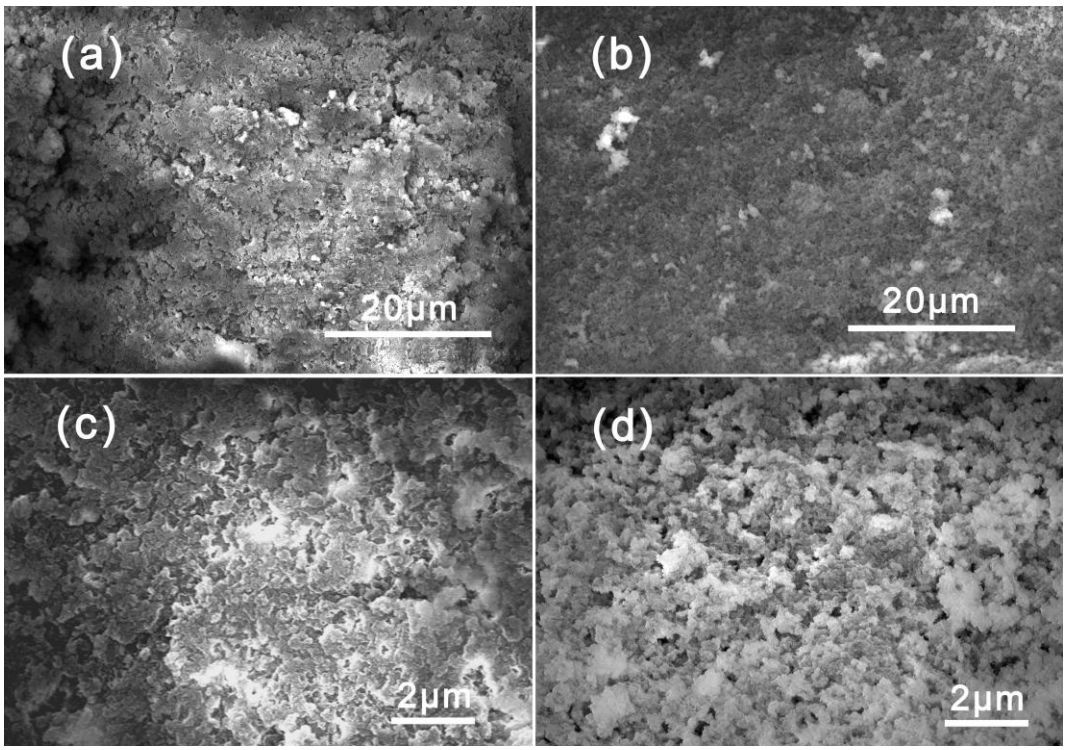

Fig. S9 SEM images of HPS-50-20 before (a, c) and after (b, d) CO_2 sorption with low and high magnification.

The sorbents before and after the 10 runs cyclic operation were observed by SEM (Fig. S8 and Fig. S9) to understand the reason of the enhanced regeneration performance by surfactant. It was found that the PEI films in surfactant-free HPS-70 displayed obvious cracks and aggregation after ten runs. On the contrary, the surfactant-promoted sorbents still retained the homogeneous surface feature. These results indicated that the aid of surfactant could maintain the unity of the PEI films. During the long term sorption-desorption cycling, the surfactant might serve as a buffering flexible matrix and confer the ability to accommodate the volume change during CO_2 sorption-desorption process, restraining the aggregation and macrophase separation of PEI molecules during the desorption process.

3. 2 Thermal stability of the sorbents, the support and Span80

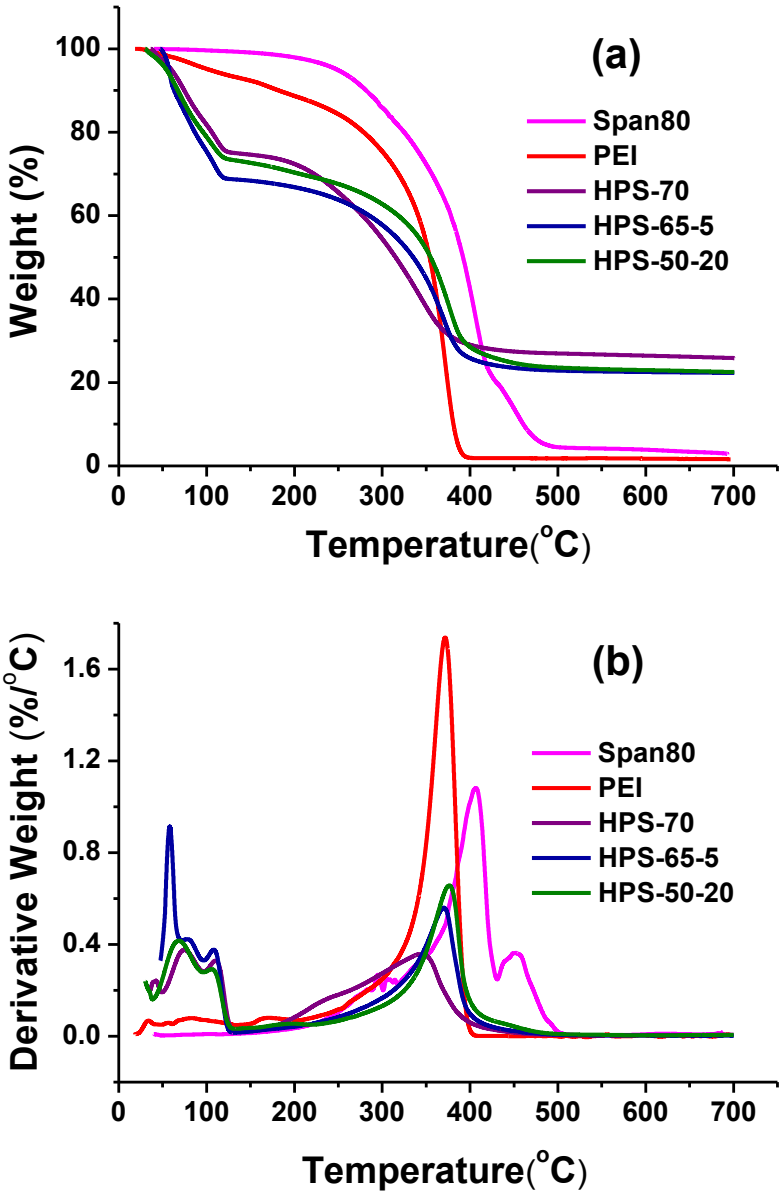

Fig.S10 TGA (a)-DTGA (b) curves of Span80, PEI, HPS-70, HPS-65-5 and HPS -50-20.

The thermal decomposition of the sorbents was monitored by a TA Instruments Q600 thermogravimetric analyzer and shown in Fig. S10. Due to the higher thermal decomposition temperature of Span80, the addition of Span80 into PEI could increase the thermal stability of the sorbents. This should be one of reasons for good regeneration performance of the surfactant-promoted sorbents, which are regenerated by temperature swing adsorption process.

References

(1) C. P. Jaroniec, M. Kruk, M. Jaroniec, A. Sayari, *J. Phys. Chem. B*, 1998, **102**, 5503.

(2) X. Wang, V. Schwartz, J. C. Clark, X. Ma, S. H. Overbury, X. Xu, C. Song, *J. Phys. Chem. C*, 2009, **113**, 7260.

(3) X. Wang, K. S. K. Lin, J. C. C. Chan, S. Cheng, *J. Phys. Chem. B*, 2005, **109**, 1763.

(4) H. Yoshitake, E. Koiso, H. Horie, H. Yoshimura, *Micropor. Mesopor. Mater.*, 2005, **85**, 183.

(5) X. Xu, C. Song, J. M. Andresen, B. G. Miller, A. W. Scaroni, *Micropor. Mesopor. Mater.*, 2003, **62**, 29.

(6) S. Satyapal, T. Filburn, J. Trela, J. Strange, *Energy Fuels*, 2001, **15**, 250-255.

(7) O. Leal, C. Bolívar, C. Ovalles, J.J. García, Y. Espidel, *Inorg. Chim. Acta*, 1995, **240**, 183-189.